The effect of eigenstrain induced by ion beam damage on the apparent strain relief in FIB–DIC residual stress evaluation

Article *in* Materials & design · December 2015

DOI: 10.1016/j.matdes.2015.12.015

CITATIONS
21

READS
232

4 authors:

Enrico Salvati
University of Oxford
47 PUBLICATIONS **186** CITATIONS
SEE PROFILE

Tan Sui
University of Surrey
85 PUBLICATIONS **402** CITATIONS
SEE PROFILE

Alexander Lunt
University of Bath
43 PUBLICATIONS **257** CITATIONS
SEE PROFILE

Alexander M Korsunsky
University of Oxford
477 PUBLICATIONS **5,255** CITATIONS
SEE PROFILE

The effect of eigenstrain induced by FIB milling on the apparent surface strain

Enrico Salvati[1], Tan Sui[1], Alexander J.G. Lunt[1], Alexander M. Korsunsky[1]

[1] Multi-Beam Laboratory for Engineering Microscopy (MBLEM), Department of Engineering Science, University of Oxford, Parks Road, Oxford OX1 3PJ, United Kingdom

Corresponding author:

Alexander M. Korsunsky

Department of Engineering Science
University of Oxford
Parks Road
Oxford OX1 3PJ
United Kingdom
Tel: +44-18652-73043
Fax: +44-18652-73010

E-Mail: alexander.korsunsky@eng.ox.ac.uk

Highlights:

1. Implantation of Ga ions during FIB milling leads to the introduction of inelastic strain that causes apparent surface strain

2. If milled features become comparable with the depth of the ion damage layer, this may affect the residual stress evaluation

3. Assessment of eigenstrain induced by FIB was performed using cantilever bending measurement.

Abstract: FIB milling using Ga ions is known to be accompanied by implantation, multiplication of material defects, material property modification (e.g. amorphisation), inelastic shrinking/swelling and residual stress generation. These processes affect the reliability of the micro-ring-core method for residual stress evaluation. Safe use of this technique requires formulating approaches that provide quantitative criteria of the method's validity. In the present study this task is accomplished by proposing a numerical model based on eigenstrain. Parametric simulations were performed to identify the extent to which the FIB-DIC micro-ring-core measurements are affected. As an example of a real and relevant material system, the procedure is applied to silicon material. The curvature of an AFM cantilever due to FIB damage was monitored, and the eigenstrain magnitude determined by matching the model to observations. Using the resulting eigenstrain profile, parametric analysis was performed in terms of the pillar radius, and the elastic strain field calculated at the pillar surface that is monitored in the FIB-DIC micro-ring-core method. An important property of the model is its versatility that allows it to be adapted to different milling conditions and geometries to determine the ultimate spatial resolution limits of the FIB-DIC method.

Keywords: FIB-DIC, ring core, FEM, eigenstrain

1. Introduction

Focused Ion beam (FIB) has become an established technique for the sample preparation at the micron- and nano-scale [1]. The main areas of application are materials science (energy, structural and functional materials), biology, coatings technology, micro-electronics, as well as many other fields. FIB allows both surface imaging and modification, i.e. the removal and/or deposition of material. Material removal is typically accomplished by bombarding the target surface with Ga^+ ions that cause the spallation of secondary ions from the sample surface.

However, the ion beam-sample interaction can lead not only to the removal of material, but also to the alteration of the defect state and/or the stress state within the target material. Alteration of residual stress state within the target material is thought to be mainly the consequence of defect, dislocation and voids evolution [2]. As discussed in [3], the damage accumulation process can be subdivided into three regimes. The first, which denotes low ion fluence, is associated to low implantation region and generates small and isolated defects. In this regime, a linear relationship has been experienced between the strain generated and the defect fraction. The beginning of loss of crystallinity is encountered at the second regime. At this stage the density of defects increases and larger ones arise from their combination. Similarly to the second, the third regime does not allow the measurement of strain since the amorphisation is predominant but, since deformation of the crystal/amorphous structure is present, the development of strain is thought to be present even during these phases.

The dynamic aspect of the interaction between the Ga ion beam and the target material can be studied by means of simulation, e.g. using SRIM code [4] or molecular dynamics (MD) [5]. MD has been extensively used to investigate a vast

range of materials processes. The simulation of Ga ion bombarding if Si surface [6-7] provided quantitative predictions of the distribution of implanted Ga ions within the Si host material, and the accompanying atomic displacements of Si atoms. A recent study has shown that Ga ion implantation during FIB milling can be reduced by means of Focused Electron Beam Induced Etching [8].

Samples that have the geometry showing a high ratio of FIB-milled surface to the overall volume are likely to be more strongly affected. For example, it is known that the preparation of samples for transmission electron microscopy (TEM) using FIB, may introduce artefacts on the surface that degrade the quality of the acquired image [9-10]. In micromechanics, the use of micro- and nano-pillar as samples for local compression testing has become widely used [11-12]. These specimens have the shape of short cylinders with dimensions that can vary from a few hundreds to thousands of nanometres in diameter. Therefore, in a number of situations the material deformation effects that accompany FIB milling cannot be neglected. Studies on copper [13] using TEM and Auger Electron Spectroscopy (AES) have shown that during FIB milling a thin amorphous layer (~50 nm) is formed in which both dislocation activity and solution hardening are inhibited. Beneath the amorphous layer produced in this way dislocation pile-up is generated, suggesting that even in the absence of additional loading some stress evolution and inelastic deformation take place. Increasing dislocation density causes changes in the mechanical properties, typically by way of either solid solution or precipitation strengthening. As a consequence, the stress required to cause plastic deformation of the pillar is increased in comparison with what would be measured for a similarly shaped ”pristine” pillar. However, dislocation dynamics simulations [14] of the affected layers and their deformation suggest that, for pillar sizes in excess of 1 μm, the local hardening effect

of the overall pillar deformation response is negligible. The thickness of the implanted layer and the depth affected by material property modification are functions of the ion beam incidence angle. The effect of FIB milling was studied on samples containing high residual stress induced by nanoindentation [15]: the morphology of indentation cracks was found to change depending on the location of milling. These observations provide supporting evidence for internal stress change due to FIB milling.

The FIB-DIC micro-ring core technique [16] is an efficient way of evaluating the residual stress present at the material surface at (sub)micron resolution. Residual stress is evaluated through FIB material removal accompanied by monitoring the surface strain changes that occur as cutting produces gradual relief from the initial state. As a ring-core marker is milled into the material surface and a micro/nano-pillar is left behind, the evolution of surface strain at the top of the pillar is monitored by Digital Image Correlation (DIC). Quantitative assessment of strain variation with milling depth allows the pre-existing residual stress to be evaluated by comparison with a model. Since the ring-core marker created in this method has geometry similar to that of a micro-pillar, it is important to take into account the above considerations concerning the effect of FIB-induced damage on the apparent stress state of the feature. Previous studies of the effect of FIB milling on material state took into account exclusively the surface effects, as well as dislocation generation and consequent material hardening. For the purpose of measuring the intrinsic elastic strain present within the sample prior to its evaluation using the FIB-DIC approach, the knowledge of additional stresses and apparent strains induced by FIB milling is required. Ga ion damage leading to amorphisation and crystal distortion is certain to cause strain modification. Furthermore, if the technique resolution is pushed towards smaller scale, when the pillar diameter reaches the order of magnitude of the FIB-

affected zone, the effect on the apparent residual stress may become dominant, having substantial impact on the reliability of the measured value.

In order to generalise the present approach, in the present study we use FE modelling to carry out numerical simulation of some putative residual strain profiles that are likely to be induced by FIB milling. Multiple conditions, in terms of the depth of the FIB-affected layer, were considered in order to provide parametric evaluation of the influence of FIB damage effect on the perceived residual stress.

Experimental evidence based on cantilever deflection (curvature) due to the presence of an external non-symmetric layer containing residual stress allows quantification of eigenstrain induced by FIB. The experiment was carried out on a commercial silicon AFM cantilever and the beam deflection observed using Scanning Electron Microscopy (SEM). The application of eigenstrain and beam bending theories allowed analytical evaluation of the intrinsic strain profile (eigenstrain) generated by FIB damage. The solution was validated by comparison with the one obtained by FEM simulation.

Eventually, the approach presented here will allow defining material-specific geometric parameters (e.g. the minimum trench diameter) to ensure that the FIB-induced effects remain negligible so that FIB-DIC method is used accurately for residual stress evaluation.

2. Eigenstrain modelling

Analysis of the interaction between a pre-existing residual stress state and the additional strain induced by the FIB-related damage during milling begins with the introduction of a numerical model that needs to be both flexible and consistent with the observations. The concept of eigenstrain [17] offers an established approach to the

modelling of residual stress effects in solids. Using pseudo-thermal strain, arbitrary eigenstrain fields can be introduced in analytical and numerical models, simply by writing the inelastic strain as follows:

$$\bar{\bar{\varepsilon}} = \bar{\bar{\alpha}}\Delta T. \quad (1)$$

i.e as the product by a fictitious temperature change ΔT of the thermal expansion coefficient tensor $\bar{\bar{\alpha}}$ that contains six independent components. By prescribing a spatially varying field $\bar{\bar{\alpha}}(\bar{\boldsymbol{r}})$, arbitrary inelastic strain distribution $\bar{\bar{\boldsymbol{\varepsilon}}}(\bar{\boldsymbol{r}})$ can be generated using a uniform temperature change. This pseudo-thermal procedure for generating eigenstrain field serves as a flexible, consistent and self-equilibrating mechanism of residual stress generation. In the framework of eigenstrain theory the task of determining the residual stress field from known eigenstrain distribution is referred to as the *direct problem*. When the residual stress or residual elastic strain distribution is known at some points within the domain of interest, and the unknown underlying eigenstrain needs to be determined, the task of finding it is known as the *inverse problem of eigenstrain theory*. This has also been treated in a number of studies using both numerical and semi-analytical approaches [18-21].

Previous studies have shown that the direct and inverse eigenstrain methodologies can be successfully applied to study a variety of cases, e.g. mechanical forming [22], autofrettaged tubes [23] and shot peened surfaces [24-25]. In some cases when the solid domain can be described mathematically using continuous functions, the direct eigenstrain problem may be solved analytically to obtain an exact solution. If not, the Finite Element Method (FEM) provides the possibility of discretising complex-shaped 2D/3D solid models, and to obtain numerical solutions.

3. Experimental Evaluation of Eigenstrain induced by Focused Ion Beam

As discussed previously, the knowledge of the strain field modification by Ga ion bombardment and subsequent damage plays an important role in the assessment of the FIB-DIC measurement accuracy. In order to estimate the amount of residual strain in the affected layer, we devised an experiment that makes use of flexible beam geometry and the measurement of curvature and deflection. The presence of a non-uniform residual stress profile, across the beam section, induces beam bending that ensures that the equilibrium of force and moment and the compatibility of total strain are satisfied simultaneously within the framework of Kirchhoff plane section kinematics. The measured radius of curvature can be correlated with the eigenstrain induced by the FIB ion damage within the beam cross section. The curvature measurement method has been successfully applied in the past for the quantification of residual stress profiles in thin coatings and films [26-27].

Atomic Force Microscope (AFM) cantilevers are slender, flexible and nearly residual stress-free micro-mechanical components. These properties of AFM cantilevers have been used previously for the determination of residual stresses generated by nickel film deposition by electroplating [28]. Our experiment is based on the observation of the cantilever deflection due to the eigenstrain introduced by FIB milling in a thin layer of material after Ga ion damage during material removal.

The angle of incidence of the ion beam on the target surface plays an important role in determining the nature of the damage cascade within the material, along with the severity and depth of the induced eigenstrain field. In most residual stress evaluation techniques that rely on material removal by FIB milling normal to the sample surface, such as the micro-ring-core FIB-DIC, the blind hole micro-drilling and the FIB slitting methods, a small incidence angle (of the order of few degrees) is formed between the ion beam and the affected surface of the remaining

material wall, e.g. a micro-pillar. Although this minimises the amount of FIB implantation, some ions are deflected and implanted deep within the material. Since the purpose of this study is to provide a conservative limit on the FIB-induced eigenstrain effect, in the present experimental assessment we consider the case of normal incidence at the angle of 90°, that can be assumed to correspond to the worst case scenario. The eigenstrain effect quantification that is obtained as a result can be considered conservative.

3.1 Experimental procedure

The cantilever used for the present experiment was a silicon AFM probe provided by Asylum Research® of type AC240TS. The main reason for choosing this sample was the absence of any coating layers on any side, the fact that no other sources of residual stress are present within the sample, and the only effect considered is that of ion beam damage and the attendant amorphisation. The micro-beam length and the dimensions of its trapezoidal cross section are depicted in Fig.1. In order to improve the accuracy of graphical evaluation of the beam curvature, a relatively large extent of the cantilever top surface (150μm) was exposed to Ga ion bombardment.

<<Figure 1 here>>

The experimental procedure consisted of the acquisition of a high resolution lateral (edge-on) image of the undeformed beam using Scanning Electron Microscope (SEM). This was followed by tilting the cantilever to align its normal with the axis of the ion beam column that is inclined at 55° to the SEM column. A thin layer was then milled at the upper surface of the cantilever using FIB energy of 30keV and ion beam

current of 0.17nA, as depicted in Fig.1. The cantilever was then again tilted so that it was viewed laterally (edge-on) by the SEM, and the thickness of the material layer removed was measured as 0.8μm. High resolution SEM imaging was also used to determine the cantilever deflection which serves as input in the analytical eigenstrain calculation. Supplementary images were taken for the purpose of observing the surface roughness after milling procedure and obtaining reliable measurement of the thickness of material removed (Fig.2).

<<Figure 2 here>>

3.2 Eigenstrain profile determination

The characterisation of the residual elastic strain induced by the presence of a thin damaged and amorphised layer can be performed by coupling the eigenstrain theory with the bending theory within an analytical formulation. This procedure has been presented and discussed in some detail by Korsunsky [25,29].

Determining the eigenstrain distribution requires an assumption to be made regarding its profile and depth-wise extent. Some recent work has shown interesting characteristics of the amorphous damage layer generated in silicon after FIB milling using Ga ion milling [30]. The residual stress profile generated by ion beam damage shows a peak close to the surface followed by a steep gradient. Simulation also predicts a possible change in the sign of residual strain, and its decay to zero value with increasing depth. The results indicate that the sign of permanent strain due to ion damage may change between positive and negative depending on the depth below the surface, ion energy, and angle of incidence. We note, however, from previous analyses of eigenstrain-induced residual stresses, that the strain caused remotely by

ion implantation is sensitive only to the integral properties of the profile, as discussed below. This allows us to proceed by reasoning that to the first approximation the eigenstrain profile can be represented by a half-Gaussian peak function. The depth extent of the damaged and amorphised layer after ion bombarding at 30keV of energy used in the present experiment reported in the literature corresponds to W =20nm. We use this parameter to set the Gaussian profile width for the eigenstrain profile. Considering the cantilever occupying the region $0 < x < h$, we describe that eigenstrain distribution below the surface $x = h$ in the form

$$\varepsilon^*_{eig}(x) = \varepsilon^*_{max}\, e^{-\frac{(x-h)^2}{2W^2}} \tag{2}$$

The calculation procedure involves the determination of the linearly varying total axial strain within the beam that is given by the sum of the elastic and inelastic strain (eigenstrain):

$$\varepsilon_{tot}(x) = \varepsilon^*_{eig}(x) + \varepsilon_{el}(x) = a + \frac{bx}{h} \tag{3}$$

The linear variation of the total strain conforms to the strain compatibility requirement for beam bending, whilst the presence of two parameters a and b allows the force and moment balance equations to be satisfied. Simple geometric analysis of the strain variation within the beam shows that the relationship between the b parameter and the beam curvature is given by

$$\frac{1}{\rho} = \frac{\mathrm{d}\varepsilon}{\mathrm{d}x} = \frac{b}{h}. \tag{4}$$

The beam curvature was measured by direct image superposition and comparison of the SEM images taken at the two significant geometrical configuration assumed; before the Ga ion exposure and after.

Since the width parameter W in the Gaussian depth profile (eq.2) is set, the task is reduced to the determination of the maximum eigenstrain value ε^*_{max}. The solution of

the problem, including the value of the beam curvature b/h, depends linearly on ε^*_{max}. The detailed calculation is shown in the Appendix.

A further validation of the eigenstrain model was conducted using FEM. A reduced three-dimensional model of the beam, taking into account its symmetry, was built and solved after imposing the eigenstrain profile found from the beam bending analysis. The contour plot of the three relevant strain components are shown in Figure 3.

<<Figure 3 here>>

The strain profiles are plotted as a function of depth into the beam cross-section are shown in Figure 4. Good match is seen between the analytical solution and the results of the FE model both in terms of cross-sectional strain distributions and the induced beam curvature.

<<Figure 4 here>>

As reported in the appendix, the maximum magnitude of eigenstrain was determined to be $\varepsilon^*_{max} = -(4.1 \pm 1.4) \times 10^{-4}$. The uncertainty was determined from the parabolic fit to the shape difference between the initial and final cantilever profile.

Silicon material, after ion exposure, usually experiences dilatation which can be represented as an introduction of positive eigenstrain [31]. Nevertheless, the experiment presented in this paper highlighted a negative eigenstrain value. The shrinkage occurred at the material can be explained by the temperature at which the ion implantation occurs. In fact, previous works reported such phenomena as function

of material temperature [32-33]. Other explanation may be sought into the effect of nano-cavities shrinkage in Silicon materials as reported in [34]. Therefore, the intense presence such features may affect the overall material response of the irradiated layer.

The ε^*_{max} value defines the scale of the entire profile of eigenstrain induced in the target material (Si) under the selected process parameters. Since eigenstrain is an intrinsic parameter of the process (Ga exposure), the knowledge of the ε^*_{max} parameter can be applied to other situations and geometries when Si ion beam milling is involved. This result is applied to the consideration of FIB-DIC pillars below, but may be used for other types of micro-structured mechanical components (e.g. MEMS).

4. Ring-core modelling and the effect on the apparent surface strain

4.1 Finite Element simulations

The linear elastic ring-core milling simulation was performed for a continuum solid material. The material was considered to be homogeneous and isotropic. It worth noting that at miniaturised components such micro-pillars may present lack of homogeneity due the presence of small voids. Nevertheless, at this stage we do not consider the affection of in-homogeneities in our model..

The elastic properties of the sample were taken to correspond to those of silicon. However, it is clear from the details of the analysis below that the elastic properties cancel out during the strain-based calculation, and are not involved in the results. Thus, systematic use of strain quantities forms a great advantage of the present procedure, since it obviates the need to consult the material constitutive law which is necessary when stress quantities need to be computed. The material was considered to

be stress-free prior to FIB milling, and the effect of the surface eigenstrain induced by ion damage was determined in terms of the surface strain change.

FIB milling causes Ga ion amorphisation in the near-surface regions of the central micro-pillar. Since ion damage typically leads to shrinking strain produced within the host material, it is assumed that FIB milling generates a compressive surface layer of eigenstrain that varies with the depth from the surface. For the purposes of current analysis, both the hoop and longitudinal (pillar extension direction) components of eigenstrain were applied within the model. In order of formulate the problem analytically, the permanent inelastic strain induced by FIB milling (eigenstrain) is assumed to follow the same half-Gaussian peak profile, obtained from the experiment seen above, as a function of the radial position (5). This profile is chosen to reflect the concentration profile following ion damage in materials that is characterised by a finite mean stopping length of the implanted ions that is associated with the width of the Gaussian peak profile.

The eigenstrain function applied in the model has the form:

$$\varepsilon^*_{\vartheta\vartheta}(r) = \varepsilon^*_{zz}(r) = \varepsilon^*_{max}\, e^{-\frac{(R-r)^2}{2W^2}}. \qquad (5)$$

Here ε^*_{max} denotes the magnitude of the maximum compressive eigenstrain introduced at the surface, and *W* represents the width of the Gaussian curve. These two parameters are depending upon the milled material properties and the FIB process parameters and are obtainable using the experimental procedure presented in the present paper.

The diameter and radius of the pillar (*D=2R*) and the radial coordinate *r* are shown in Fig.5(a). A schematic representation of the FIB milling process and the position of application of the eigenstrain profile are depicted in Fig. 5(b).

<< Figure 5 here >>

Axisymmetric modelling of the ring-core milling process was accomplished using the FEM suite ABAQUS© v.12. The model was subdivided into regions, allowing the material removal by FIB milling to be modelled by modifying the properties of selected material domains by setting their properties to that of "air". The mesh was refined in the regions where high stress gradients were expected,

4.2 Parametric analysis

The parametric analysis was conducted by varying the width of the Gaussian curve with respect to the other principal length scale of the problem, the pillar radius. The dimensionless parameter that describes this ratio is $w=W/R$. Parametric characterisation was achieved by running multiple simulations for milling depths h/D between zero and unity, and considering the apparent strain change at the pillar surface as input for residual stress interpretation using the FIB-DIC procedure [15]. The dimensionless parameter that was introduced in order to reflect the strain change induced by FIB damage was the strain calculated at the centre of the pillar surface. Due to the linearity of the eigenstrain FEM problem, the elastic strain at pillar surface scales proportionally to the maximum eigenstrain value imposed, ε^*_{max}. It is important to note that during milling the residual elastic strain that arises at the pillar surface varies as a function of radial position, and also depends on the geometric relationships between pillar radius R, the milling depth h, and the eigenstrain distribution width parameter, W. However, for the purposes of numerical presentation of the results it is convenient to select a single dimensionless parameter to represent the milling-induced straining of the pillar surface.

One suitable dimensionless expression has the form $| e_{rr}(0)/\varepsilon^*_{max} |$, where $e_{rr}(0)$ denotes the residual elastic strain arising at the centre of the pillar surface, and ε^*_{max} has been defined earlier in eq.(2).

Once the effect of FIB milling is calibrated, by means of the numerical model described below, the error introduced into the FIB-DIC residual stress evaluation can be quantified. Then, this defines the threshold in terms of the minimum pillar dimensions for which sample residual stress effects still dominate over the FIB-induced strain effects, sufficiently to obtain reliable residual stress measurement.

In FIB-DIC measurement, the DIC measurement is performed on the top stub surface calculating an average strain value over a certain area that is smaller than the entire one (Fig.5b). For this reason we propose also an alternative dimensionless expression to represent the consequence of the Ga damage. From the numerical results, the average value along the radial direction can be evaluated and hence we obtain a value which can be compared with the one from DIC analysis. In this case we considered the mean value of $e_{rr}(r)$ evaluated between *r=0* and *r=0.9R*; we called it $< e_{rr} >$.This means that the average was done over a reduced surface of the stub like DIC analysis as shown in Fig.5(b). Once again the mean value was turned into a dimensionless quantity dividing by the maximum eigenstrain value imposed, ε^*_{max}. The quantity then assumed the form of $< e_{rr} > /\varepsilon^*_{max}$.

This secondary representation allows the direct quantification of the amount of strain that affects the FIB-DIC measure. Once a threshold of acceptability of this effect is set, in terms of $< e_{rr} >$. the minimum pillar dimension can be deduced.

To a good approximation, the parametric outcomes can be summarised using polynomial or power fitting functions, as reported in the figures.

4.3 Results and discussion

General observations

The results of the axisymmetric FE model can be seen in 3D and in the form of the contour plot (Fig.6) showing the hoop stress component. The simulation has been performed assuming that no residual stress is present prior to milling. The pillar radial contraction that takes place due to the relief of residual tensile stress is apparent.

<< Figure 6 here >>

The plot of the radial strain as a function of the radial position is shown in Fig.7 for the top surface, providing the visualisation of strain change in the affected area. In this analysis we do not take into account the perceived strain changing during the whole milling process. Thus, the elastic strain field we consider is referred to the last milling step, then at the depth h/D=1. This strain change function has been normalised, both in ordinate and abscissa, with the maximum value assumed. Seven different W/R ratios were analysed and plot; starting for a very narrow Gaussian shape W/R=2.5×10^{-3} to the wider one W/R=0.1

<< Figure 7 here >>

Using the results of FEM analysis it was possible to evaluate the elastic strain at the centre of the micro-pillar, and the average value across the reduced area spanning 90% of the entire radius of the pillar. On this basis, a function was obtained that shows the ion damage effects on the FIB-DIC ring-core measurement (Fig.8a and 8b).

In order to identify the minimum pillar radius, an example determination of the threshold pillar radius R^* is shown.

<< Figure 8 here >>

To perform reliable residual stress measurement using the FIB-DIC micro-ring-core technique, the error due to Ga ion damage during FIB milling must be controlled. This information provides a guide to the experimentalist during setup of the experiment. For example, from the point of view of the FIB-DIC procedure, the probe current and voltage are process parameters that influence the outcomes in terms of the induced ion damage. Although it is clear that reducing ion beam voltage and current lead to the reduction of ion damage effects, this also leads to slower material removal rates, making the experimental measurements more time consuming. Therefore, in practice an optimal compromise between these objectives needs to be found. The present results provide a firm quantitative basis for optimising the experimental conditions.

The half Gaussian function shape, imposed by means of eigenstrain, is reflected in both the hoop and radial stress components that assume similar general trends (Fig.7). As expected, the predominant FIB damage induced effect is present in the vicinity of the surface exposed to Ga Ions. If the FIB damage is localised primarily within the micro-pillar skin, a negligible effect is perceivable at the centre zone of the top surface of the micro-pillar. For values of W/R higher than ~0.005, the consequence of the induced effect becomes relevant, and then the entire micro-pillar is subjected to additional elastic residual strain.

The function shown in Fig. 8(a) and Fig. 8(b) confirms the expected trend, in that smaller pillar diameters correspond to high values of the perceived strain at the top surface of the pillar. In order to make this effect negligible on the global FIB-DIC measure, it is necessary define a threshold of acceptability. This threshold defines the conditions when the micro ring-core method can be applied for the determination of residual stress ignoring the influence of FIB ion damage.

Fig.8b displays the variation of the average strain determined by DIC in the region of interest defined by the 90% radial extent of the micro-pillar surface. This perceived strain value is related directly to the experimental implementation of the FIB-DIC micro-ring-core procedure, and thus provides the most relevant and direct basis for setting the threshold for the FIB-induced straining effect. Once the FIB milling parameters are defined, then so are the parameters W and ε^*_{max}. This determines the intersection of the strain-induced curve with the chosen threshold, and thus provides the basis for determining the minimum acceptable pillar radius, R^* (Fig.8).

It is worth noting that the imposition of the same magnitude of threshold, for the two different approaches, leads to different pillar dimension evaluation. In fact, in Fig.8 it is possible to observe the greater value of the ratio W/R* in the case when the induced radial strain at the pillar centre is considered (Fig.8a) compared to use of the strain averaged over the reduced area (Fig.8b). This means that the latter defines a greater minimum pillar size, and hence is more conservative.

Application to silicon material

Once the eigenstrain induced by Focused Ion Beam was quantified through the experimental procedure presented in this paper, parametric analysis can be used to assess the impact on the residual strain measurement using FIC-DIC. This analysis is

fully valid only if identical FIB process parameters were used both in the eigenstrain determination experiment, and in the FIB-DIC measurement.

The parameter that defines the maximum magnitude of eigenstrain was evaluated to be $\varepsilon^*_{max} = -4.1 \cdot 10^{-4}$. Hence, the analysis of the apparent strain on the stub surface is reported now as a function of the pillar radius alone (Fig.9).

The choice of an appropriate threshold is crucial in this analysis. The fundamental idea is that the effect of ion damage must be negligible in terms of the magnitude of the apparent residual strain that is causes. Since this last one cannot be known a priori, we decided to compare this effect with the error due to DIC analysis. The in-house Digital Image Correlation software built for the purpose of residual strain evaluation can deliver the accuracy of strain relief determination the order 10^{-4} or better. Accordingly, we choose a threshold equal to half of the DIC accuracy, namely, 0.5×10^{-4}.

<<Figure 9 here>>

Assuming the depth of material affected by ion beam induced amorphisation to be known, the choice of admissible value of induced strain (threshold) and the knowledge of the maximum amplitude of induced eigenstrain allowed the determination of the lower limit for the micro-pillar radius. As shows in Fig.9, this evaluation led to the conclusion that the FIB damage effect becomes significant when micro-pillar radii become less than 1μm. Particularly, if only the centre of the top micro-pillar surface is considered to be representative of the entire strain field, the lower bound for the admissible micro-pillar radius turns out to be even smaller, namely ~0.5μm.

5. Conclusions

Precise evaluation of the consequence of FIB milling is important in the context of the ongoing quest for feature miniaturization. The success of nanoscale sample preparation by ion beam machining is determined not only by the ability to create the desired geometric features, but also by the degree to which the material properties are preserved within the small volumes of interest. When the sought properties and structure are modified either partially or completely, the results obtained can be subject to aberration, or may become completely misleading, as for example as a consequence of ion beam-induced amorphisation of single crystals.

Residual stress is an important property of material state that is often difficult to determine at the micron scale, e.g. due to significant amount of plastic deformation [35-36]. One of the challenges to progressive miniaturization of FIB-DIC ring-core measurement is the FIB-induced Ga ion damage that affects the strain measured at the surface.

We quantified this interaction via a numerical simulation that determined the FIB-induced strain effect on the perceived surface strain, and derived a basis for the evaluation of lower bound pillar radius acceptable for stress evaluation. The numerical analyses presented here represented predictions of the impact that FIB milling can have on micro-ring-core residual stress evaluation. Furthermore, we carried out novel experiments in which the effect of ion beam damage was quantified (in terms of the maximum eigenstrain induced). Once the maximum magnitude of eigenstrain was found, and its depth extent and the residual stress evaluation error threshold were set, parametric analysis presented here was used as a tool for FIB-DIC experiment design: lower bounds on the micro-pillar diameters were set. One

important aspect of the present model is its flexibility that allows it to be re-run for arbitrary depth of Ga ion damage depending on the substrate material, ion energy and flux, angle of incidence, etc., leading to different dependence of eigenstrain on the depth from the surface.

The experimental procedure reported in this paper for the quantification of eigenstrain is an efficient way of characterising the residual stress field arising from the interaction between the ion beam and the target material.

The present paper also contains specific results for the lower bound pillar sizes in the case where the target material is silicon. To ensure aberration-free residual stress evaluation, the pillar radius should not be smaller than 1μm. A less conservative way of determining this value, considering only the value of strain induced at the centre of the pillar, leads to a minimum radius of ~0.5μm.

Appendix

The total strain is the result of two contributions: eigenstrain generated by the material amorphisation, and the elastic strain generated within the material to accommodate the presence of eigenstrain, and maintain strain compatibility within the cantilever. This total strain present in beam cross section can be represented as a linear function of its thickness according to Kirchhoff's hypothesis of plane normals:

$$\varepsilon_{tot}(x) = \varepsilon^*_{eig}(x) + \varepsilon_{el}(x) = a + \frac{bx}{h} \tag{6}$$

The function describing the eigenstrain profile is assumed to have the form:

$$\varepsilon^*_{eig}(x) = \varepsilon^*_{max}\, e^{-\frac{(x-h)^2}{2W^2}} \tag{7}$$

Therefore, the elastic strain can be expressed as:

$$\varepsilon_{el} = \varepsilon_{tot} - \varepsilon^*_{eig} = a + \frac{bx}{h} - \varepsilon^*_{max}\, e^{-\frac{(x-h)^2}{2W^2}} \tag{8}$$

The conditions of Force and Moment equilibria across the beam lead to the following equations:

$$\boldsymbol{F} = \int_{\boldsymbol{A}} \left(\varepsilon_{tot} - \varepsilon^*_{eig}\right) dA = \int_0^h \int_0^{f(x)} \left[a + \frac{bx}{h} - \varepsilon^*_{max}\, e^{-\frac{(x-h)^2}{2W^2}}\right] dy\, dx = 0 \tag{9}$$

$$\boldsymbol{M} = \int_{\boldsymbol{A}} \left(\varepsilon_{tot} - \varepsilon^*_{eig}\right) x\, dA = \int_0^h \int_0^{f(x)} \left[a + \frac{bx}{h} - \varepsilon^*_{max}\, e^{-\frac{(x-h)^2}{2W^2}}\right] x\, dy\, dx = 0 \tag{10}$$

These expressions involve integration over the domain occupied by the beam cross-section. The geometrical properties of this cross-section are known, as shown in (Fig.10 and Tab.1).

<<Figure 10 here>>

α [mm]	**β [mm]**	**h [mm]**
0.021	0.0354	0.0020

Table 1. Cantilever cross section dimensions

The upper limit of integration in y is defined by the oblique "bevel" edge. This can be represented by the equation:

$$f(x) = \frac{x(\alpha - \beta)}{2h} + \frac{\beta}{2} \tag{11}$$

Coefficient b of the total strain equation is directly related to the beam curvature through the following relation:

$$k = \frac{b}{h} \tag{12}$$

The curvature is the inverse of the beam bending radius ρ. This was found to be equal to (40.78±21.21) mm. Hence, b can be determined as:

$$b = h\,k = \frac{h}{\rho} = \frac{0.002}{40.78} = 4.9 \times 10^{-5} \tag{13}$$

The coefficient that defines the width of the Gaussian function is also known from the literature, as noted before. Therefore, the system of equations (9) and (10) can be solved numerically for the coefficients a and ε^*_{max} to obtain, respectively, the values of -1.5×10^{-5} and -4.1×10^{-4}, determined with the relative accuracy of ~35%.

Acknowledgements

AMK acknowledges funding received by MBLEM through EU FP7 project iSTRESS (604646).

References

[1] K. Topolski, P. Wiecinski, S. Zygmunt. Progress in the characterization of explosively joined Ti/Ni bimetals, MATERIALS & DESIGN 63, 479-487 (2014)

[2] J. M. Glasko, R. G. Elliman, J. Zou, D. J. H. Cockayne, J. D. Fitz Gerald. Strain and defect microstructure in ion-irradiated GeSi/Si strained layers as a function of annealing temperature. Applied Physics Letters Volume 73, Number 6 (1998)

[3] S. Decoster and A. Vantomme. Implantation-induced damage in Ge: strain and disorder profiles during defect accumulation and recovery. J. Phys. D: Appl. Phys. 42 (2009) 165404 (10pp). doi:10.1088/0022-3727/42/16/165404

[4] J. F. Ziegler, "Handbook of Stopping Cross Sections for Energetic Ions in All Elements," vol. 5 of series "Stopping and Ranges of Ions in Matter," Pergamon Press, New York (1980).

[5] C. L. Liu and S. J. Plimpton. Molecular-dynamics simulations of grain-boundary diffusion in Al using embedded-atom method potentials, J Materials Research, 10, 1589-1592 (1995).

[6] L. Pelaz, L. A. Marques, J. Barbolla. Ion-induced amorphization and recrystallization in silicon. Applied Physics Review. Journal of Applied Physics. Vol 96, n.11 (2004)

[7] Michael F. Russo, Mostafa Maazouz, Lucille A. Giannuzzi, Clive Chandler, Mark Utlaut and Barbara J. Garrison. Gallium-Induced Milling of Silicon: A Computational Investigation of Focused Ion Beams. Microsc. Microanal. 14, 315–320, 2008 doi:10.1017/S1431927608080653

[8] P Roediger, H D Wanzenboeck, S Waid, G Hochleitner and E Bertagnolli. Focused-ion-beam-inflicted surface amorphization and gallium implantation—new insights and removal by focused-electron-beam-induced etching. Nanotechnology 22 (2011) 235302 (10pp)

[9] J.P. McCaffrey, M.W. Phaneuf, L.D. Madsen. Surface damage formation during ion-beam thinning of samples for transmission electron microscopy. Ultramicroscopy 87 (2001) 97–104

[10] V. Delaye, F. Andrieu, F. Aussenac, C. Carabasse. In-line FIB TEM sample preparation induced effects on advanced fully depleted silicon on insulator transistors. EMC 2008 14th European Microscopy Congress 1–5 September 2008, Aachen, Germany 2008, pp 659-660

[11] O. V. Kuzmin, Y. T. Pei, J. T. M. De Hosson. Nanopillar Fabrication with Focused Ion Beam Cutting. Microsc. Microanal. 20, 1581-1584, (2014)

[12] N.L. Okamoto, M. Inomoto, H. Adachi, H. Takebayashi, H. Inui. Micropillar compression deformation of single crystals of the intermetallic compound f-FeZn13. Acta Materialia 65 (2014) 229-239

[13] D. Kiener, C. Motz, M. Rester, M. Jenko, G. Dehm. FIB damage of Cu and possible consequences for miniaturized mechanical tests. Materials Science and Engineering A 459 (2007) 262–272

[14] Jaafar A. El-Awady, Christopher Woodward, Dennis M. Dimiduk and Nasr M. Ghoniem. Effects of focused ion beam induced damage on the plasticity of micropillars. Physical Review B 80, 104104 (2009)

[15] B J Inkson, D Leclere, F Elfallagh, B Derby. The effect of focused ion beam machining on residual stress and crack morphologies in alumina. Journal of Physics: Conference Series 26 (2006) 219–222

[16] A.M. Korsunsky, M. Sebastiani, E. Bemporad. Focused ion beam ring drilling for residual stress evaluation. Material Letters 63, 1961-1963, (2009).

[17] A.M. Korsunsky. Eigenstrain analysis of residual strains and stresses, The Journal of Strain Analysis for Engineering Design. 01/2009; 44(1):29-43. DOI:10.1243/03093247JSA423

[18] T. S. Jun and A.M. Korsunsky. Evaluation of residual stresses and strains using the Eigenstrain Reconstruction Method. International Journal of Solids and Structures Volume 47, Issue 13, 15 June 2010, Pages 1678–1686.

[19] M.E. Kartal, R. Kiwanuka, F.P.E. Dunne. Determination of sub-surface stresses at inclusions in single crystal superalloy using HR-EBSD, crystal plasticity and inverse eigenstrain analysis. Int. J. of Solids and Structures, Vol. 67–68, 15 Aug. 2015, Pages 27-39

[20] H.T. Luckhoo, T.-S. Jun, A.M. Korsunsky. Inverse eigenstrain analysis of residual stresses in friction stir welds. Mesomechanics. Volume 1, Issue 1, July 2009, Pages 213–216.

[21] R. Nedin, A. Vatulyan. Inverse problem of non-homogeneous residual stress identification in thin plates. Int. J. of Solids and Struct. Volume 50, Issue 13, 15 June 2013, Pages 2107–2114

[22] A.M. Korsunsky, G.M. Regino,D.P. Latham, H.Y. Li, M.J. Walsh. Residual stresses in rolled and machined nickel alloy plates: Synchrotron X-ray diffraction measurement and three-dimensional eigenstrain analysis. Journal of Strain Analysis for Engineering Design. Volume 42, Issue 1, 2007, Pages 1-12

[23] A.M. Korsunsky. Residual elastic strains in autofrettaged tubes: elastic-ideally plastic model analysis. Journal of Engineering Materials and Technology – Transactions of the ASME, 129 (1) (2007), pp. 77–81

[24] A.M. Korsunsky. On the modelling of residual stresses due to surface peening using eigenstrain distributions. Journal of Strain Analysis for Engineering Design, 40 (8) (2005), pp. 817–824

[25] A.M. Korsunsky. Residual elastic strain due to laser shock peening: modelling by eigenstrain distribution. J. Strain Analysis. Vol. 41 No.3. (2005) DOI: 10.1243/03093247JSA141.

[26] R. Schöngrundnera, R. Tremlb, T. Antretterc, D. Kozica, W. Eckera, D. Kienerb, R. Brunnera. Critical assessment of the determination of residual stress profiles in thin films by means of the ion beam layer removal method. Thin Solid Films. Volume 564, 1 August 2014, Pages 321–330

[27] L.M. Jiang, J. Peng, Y.G. Liao, Y.C. Zhou, J. Liang, H.X. Hao, C. Lu. A modified layer-removal method for residual stress measurement in electrodeposited nickel films. Thin Solid Films 519 (2011) 3249–3253

[28] S.-H. Kim. Mismatch Strain and Residual Stress of Freestanding Electroplated Ni Thin Film. Japanese J. of Applied Physics, 49 (2010)

[29] A.M. Korsunsky. On the modelling of residual stresses due to surface peening using eigenstrain distributions. J. Strain Analysis. Vol. 40 No. 8 (2005). DOI: 10.1243/030932405X30984

[30] L. Pastewka, R. Salzer, A. Graff, F. Altmann, M. Moseler. Surface amorphization, sputter rate, and intrinsic stresses of silicon during low energy Ga+ focused-ion beam milling. Nuclear Instruments and Methods in Physics Research B 267 (2009) 3072–3075

[31] Saitoh, K. ; Nakao, Setsuo ; Niwa, H. Surface Swelling of MeV Si Ion Implanted Silicon. Ion Implantation Technology Proceedings, 1998 International Conference on (Volume:2).

[32] Saitoh, K. ; Nakao, Setsuo. Mechanical strain and damage in Si implanted with O and N ions at elevated temperatures: Evidence of ion beam induced annealing. Saitoh, K. ; Nakao, Setsuo ; Niwa, H.

[33] A. Battaglia, F. Priolo and E. Rimini. Influence of doping on ion-induced growth and shrinkage of partial damage in silicon. Nuclear Instruments and Methods in Physics Research BS9/40 (1991) 382-385

[34] X. Zhu and Z. Wang. Nanoinstabilities as revealed by shrinkage of nanocavities in silicon during irradiation. Int. J. Nanotechnology, Vol. 3, No. 4, 2006.

[35] F. Hofmann, B. Abbey, L. Connor, N. Baimpas, X. Song, S. Keegan, A.M. Korsunsky. Imaging of grain-level orientation and strain in thicker metallic

polycrystals by high energy transmission micro-beam Laue (HETL) diffraction techniques. International Journal Of Materials Research. Volume: 103. Issue: 2. Pages: 192-199. DOI: 10.3139/146.110660

[36] A.M. Korsunsky, M.R. Daymond, K.E. James. The correlation between plastic strain and anisotropy strain in aluminium alloy polycrystals. Materials Science And Engineering A-Structural Materials Properties Microstructure And Processing Volume: 334. Issue: 1-2. Pages: 41-48. Art. Number: PII S0921-5093(01)01780-4 Published: SEP 1 2002

Captions

Figure 1. Schematic representation of the cantilever geometry and its dimensions. Units in micrometres.

Figure 2. SEM images of the cantilever lateral view. a) Prior milling. b) After milling.

Figure 3. Contour plots of strain within the beam cross-section: a) total strain. b) elastic strain. c) eigenstrain.

Figure 4. Total strain, elastic strain and eigenstrain within the beam cross-section obtained from a) the analytical solution, and b) the FEM simulation.

Fig. 5. FIB affected area representation and modelling. a) Coordinate system representation. b) SEM image taken during FIB milling. b) FIB milling process schematization: Highlighted in red the regions where the Ion damage appears. The half Gaussian profile represents the eigenstrain imposed at the geometry.

Fig. 6. Radial residual elastic strain due to FIB ring-core milling, depth ratio a) h/D=0.5 and b) h/D=1

Fig. 7. Normalised Elastic strain along the radial direction for various W/R ratios

Fig. 8. FIB induced effect on the stub top surface. Examples of minimum pillar diameter determination. a) Considering the value of the elastic radial strain at the centre of the stub surface as most relevant quantity. b) Considering the average over the 90% of the reduced radius as most relevant quantity.

Figure 9. Minimum micro-pillar radius determination. a) Based on the apparent strain at the centre. b) Based on the average strain within the area of 90% radial extension upon at the micro-pillar top surface.

Figure 10. Cantilever cross-section representation

Figures

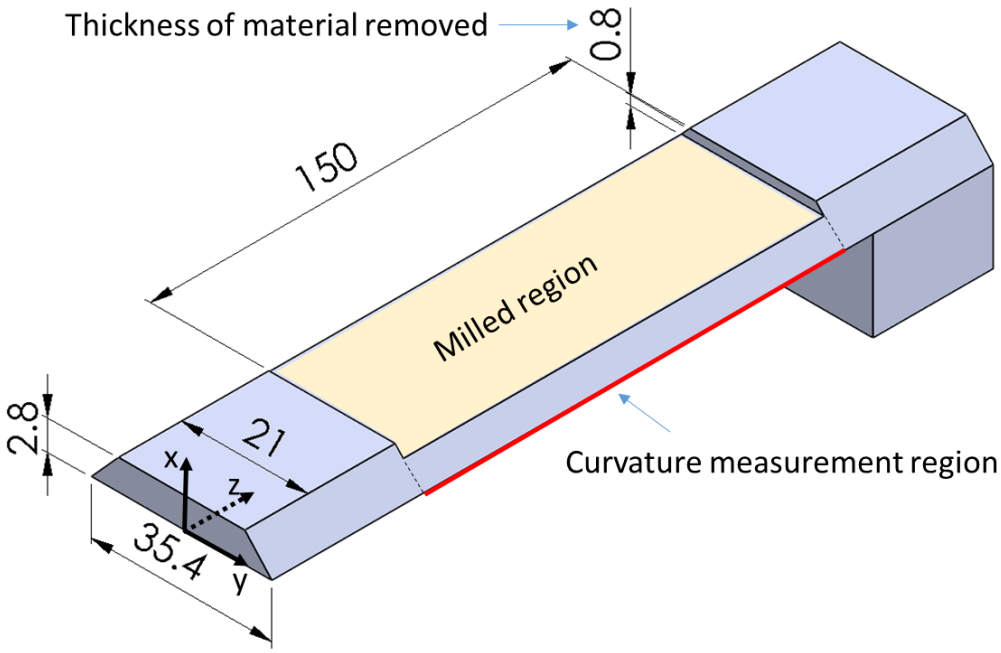

Figure 1. Schematic representation of the cantilever geometry and its dimensions. Units in micrometres.

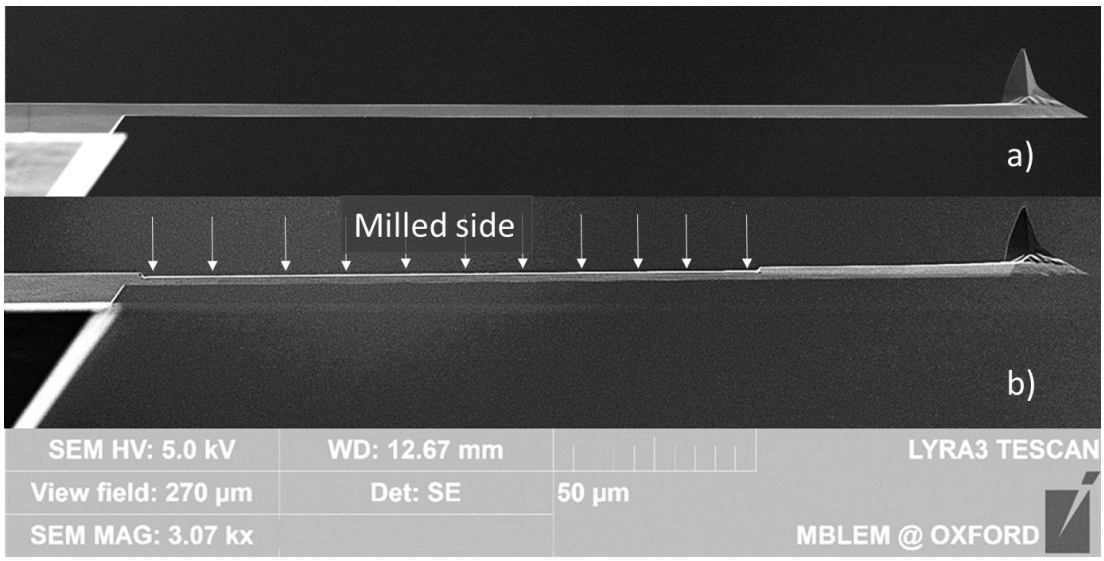

Figure 2. SEM images of the cantilever lateral view. a) Prior milling. b) After milling.

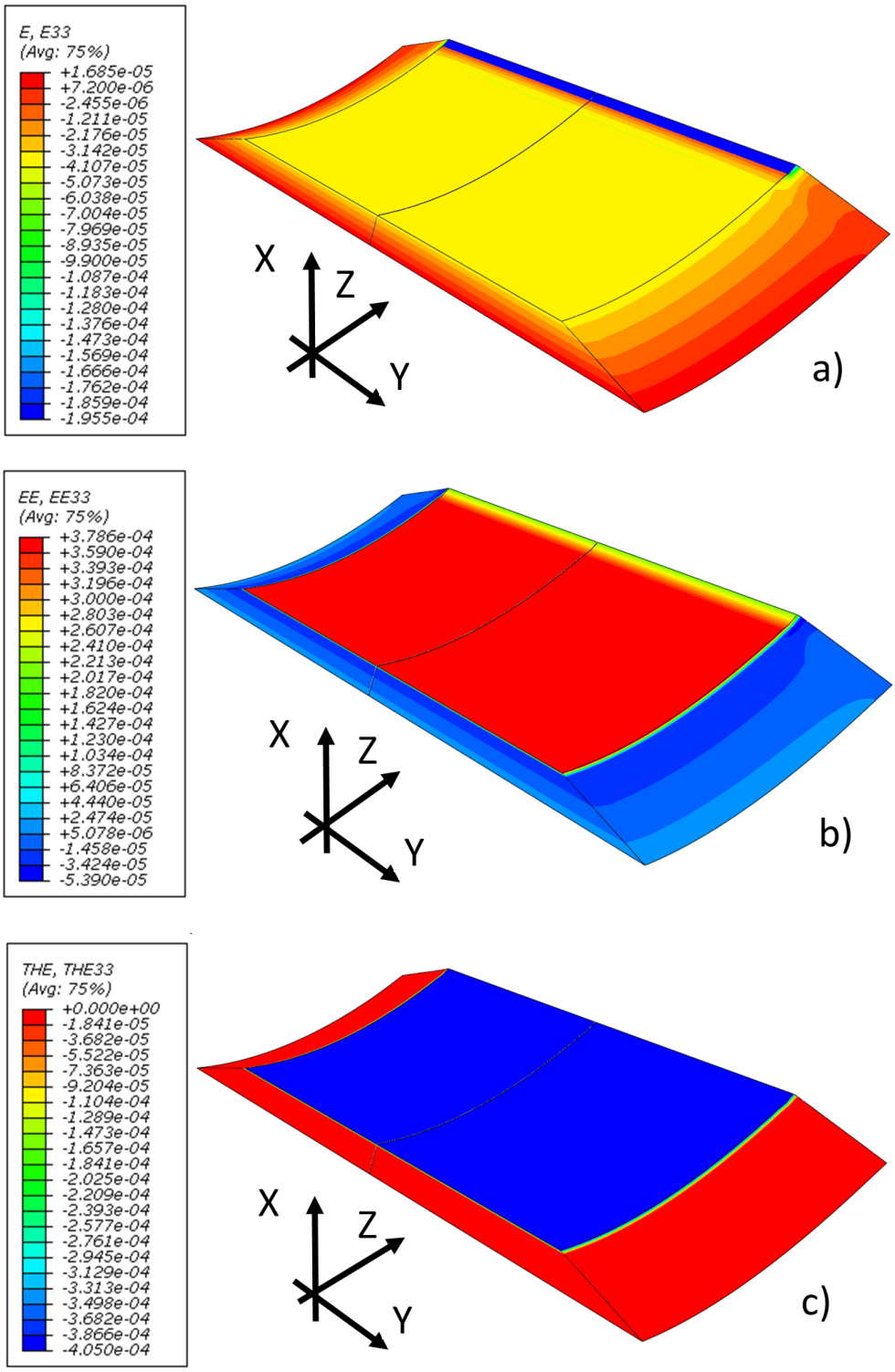

Figure 3. Contour plots of strain within the beam cross-section: a) total strain. b) elastic strain. c) eigenstrain.

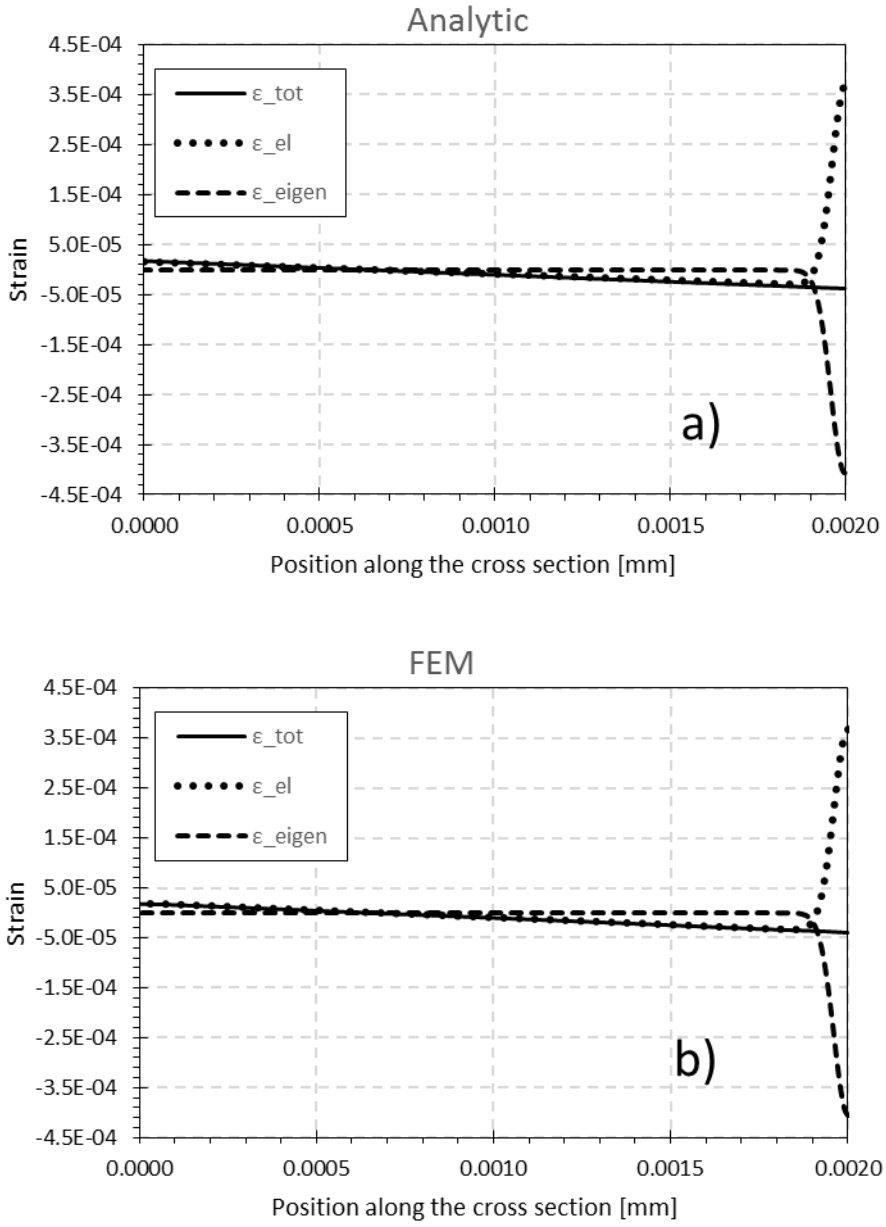

Figure 4. Total strain, elastic strain and eigenstrain within the beam cross-section obtained from a) the analytical solution, and b) the FEM simulation.

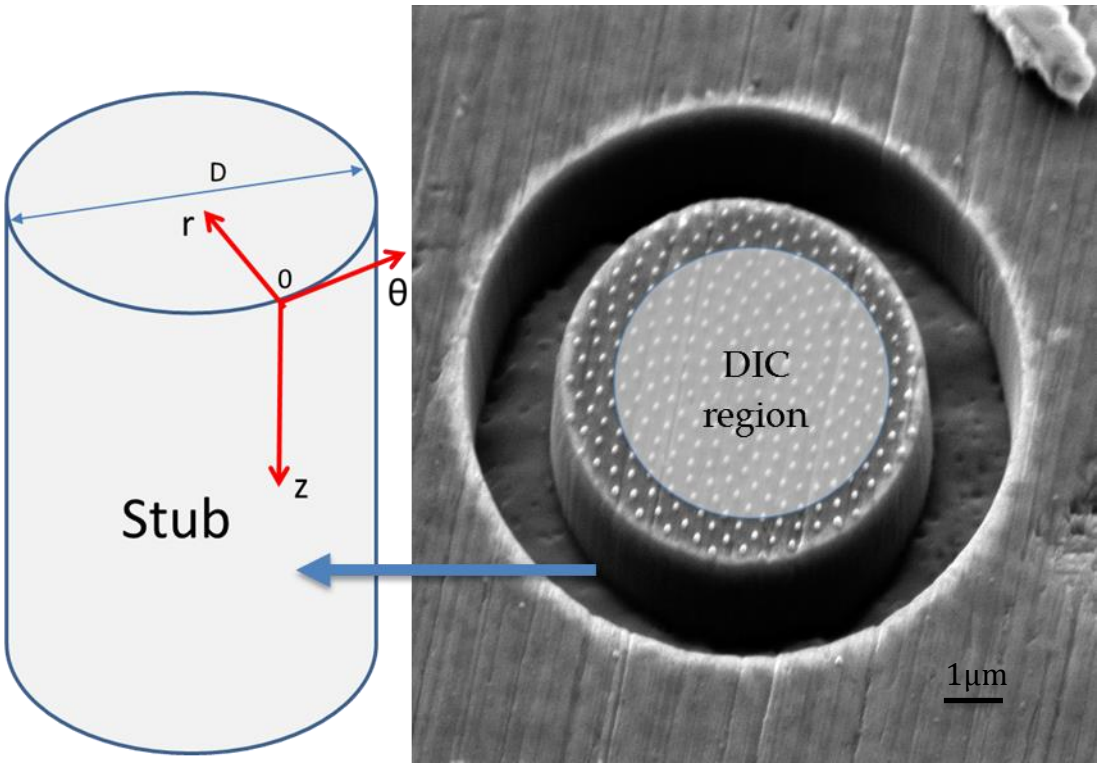

a) **b)**

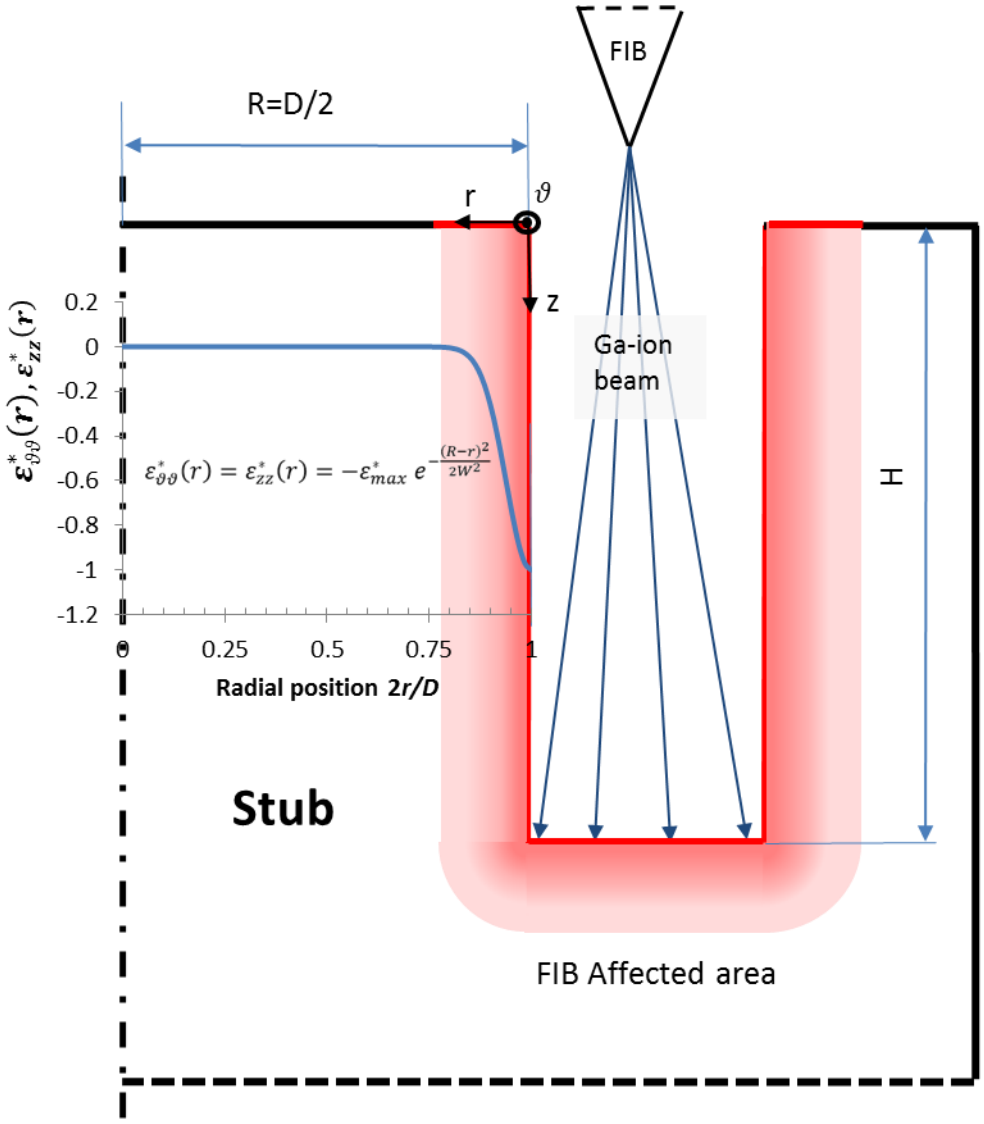

c)

Fig. 5. FIB affected area representation and modelling. a) Coordinate system representation. b) SEM image taken during FIB milling. b) FIB milling process schematization: Highlighted in red the regions where the Ion implantation appears. The half Gaussian profile represents the eigenstrain imposed at the geometry.

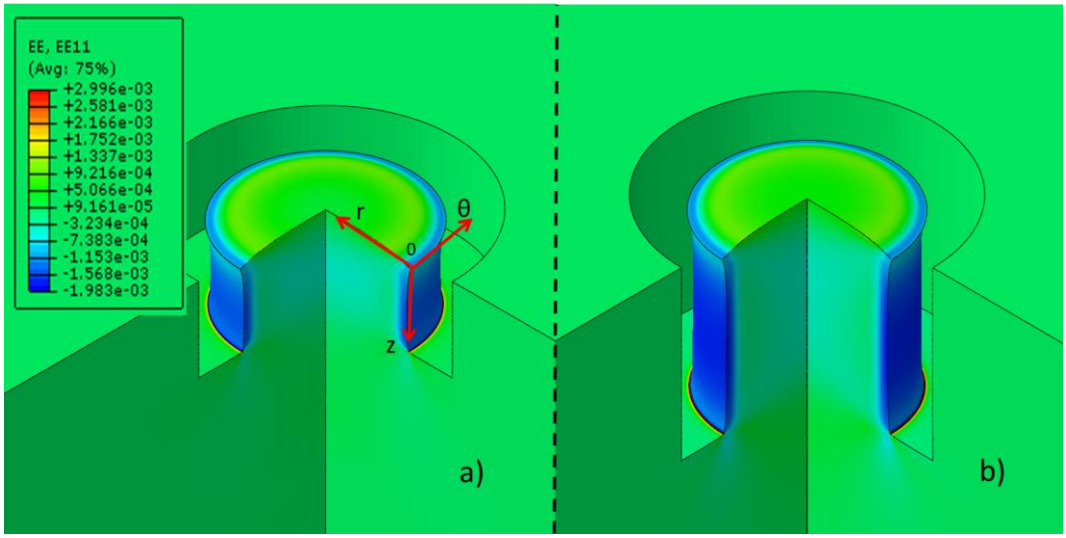

Fig. 6. Example of radial residual elastic strain due to FIB ring-core milling imposing an eigenstrain profile with W/R=0.1 as extension, depth ratio a) h/D=0.5 and b) h/D=1

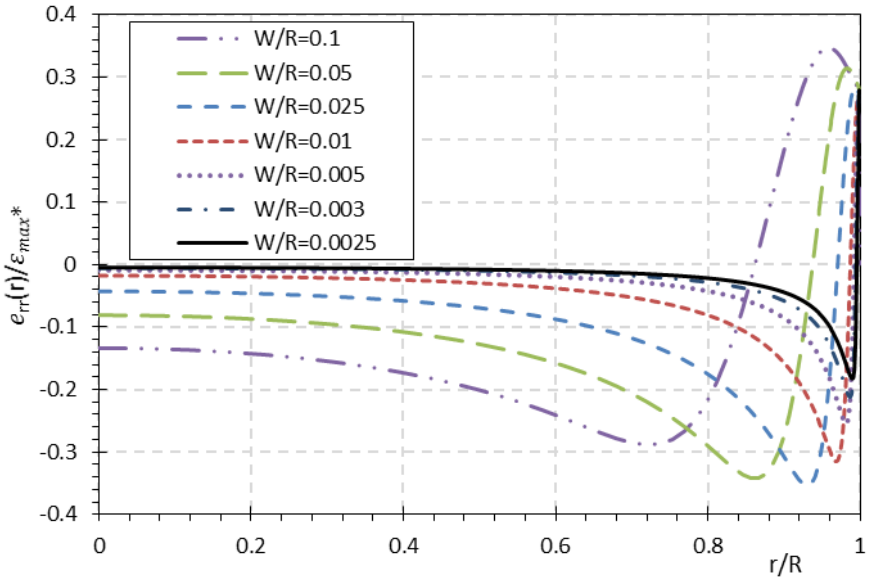

Fig. 7. Normalised Elastic strain along the radial direction for various *W/R* ratios at depth of milling h/D=1

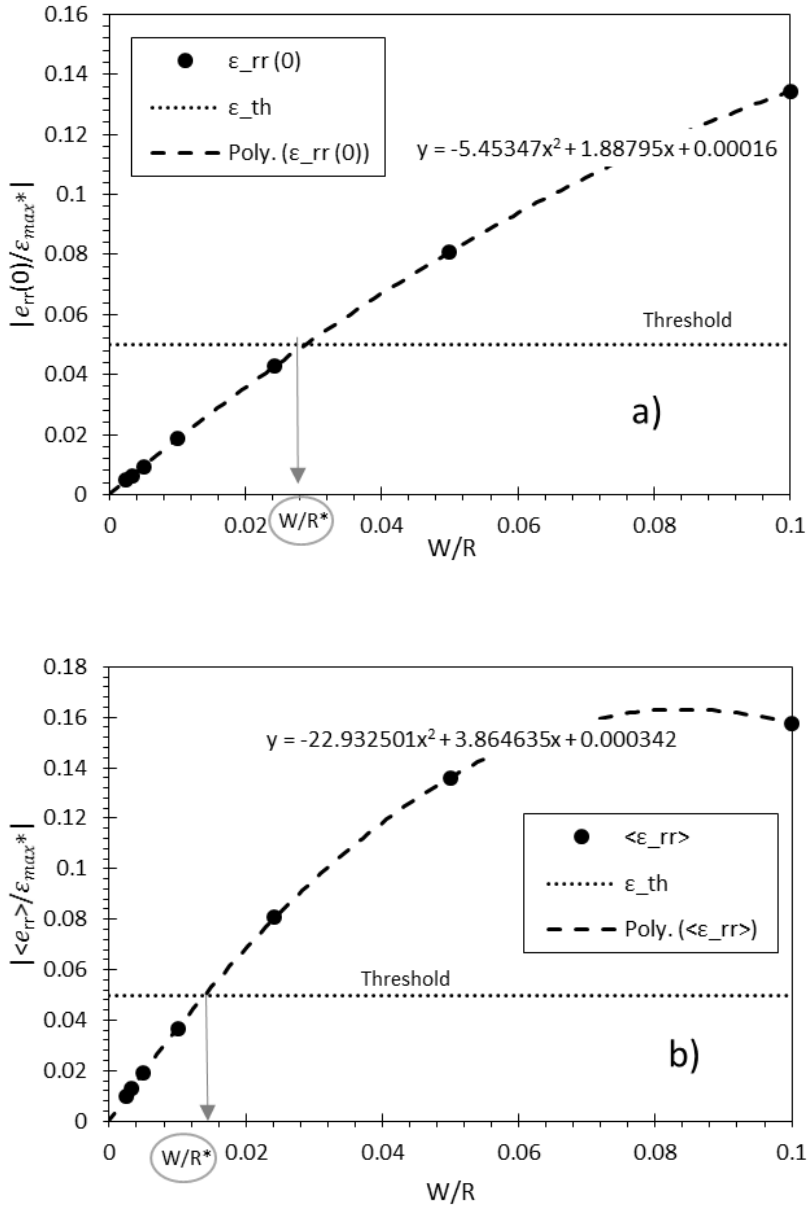

Fig. 8. FIB induced effect on the stub top surface. Examples of minimum pillar diameter determination. a) Considering the value of the elastic hoop strain at the centre of the stub surface as most relevant quantity. b) Considering the average over the 90% of the reduced radius as most relevant quantity.

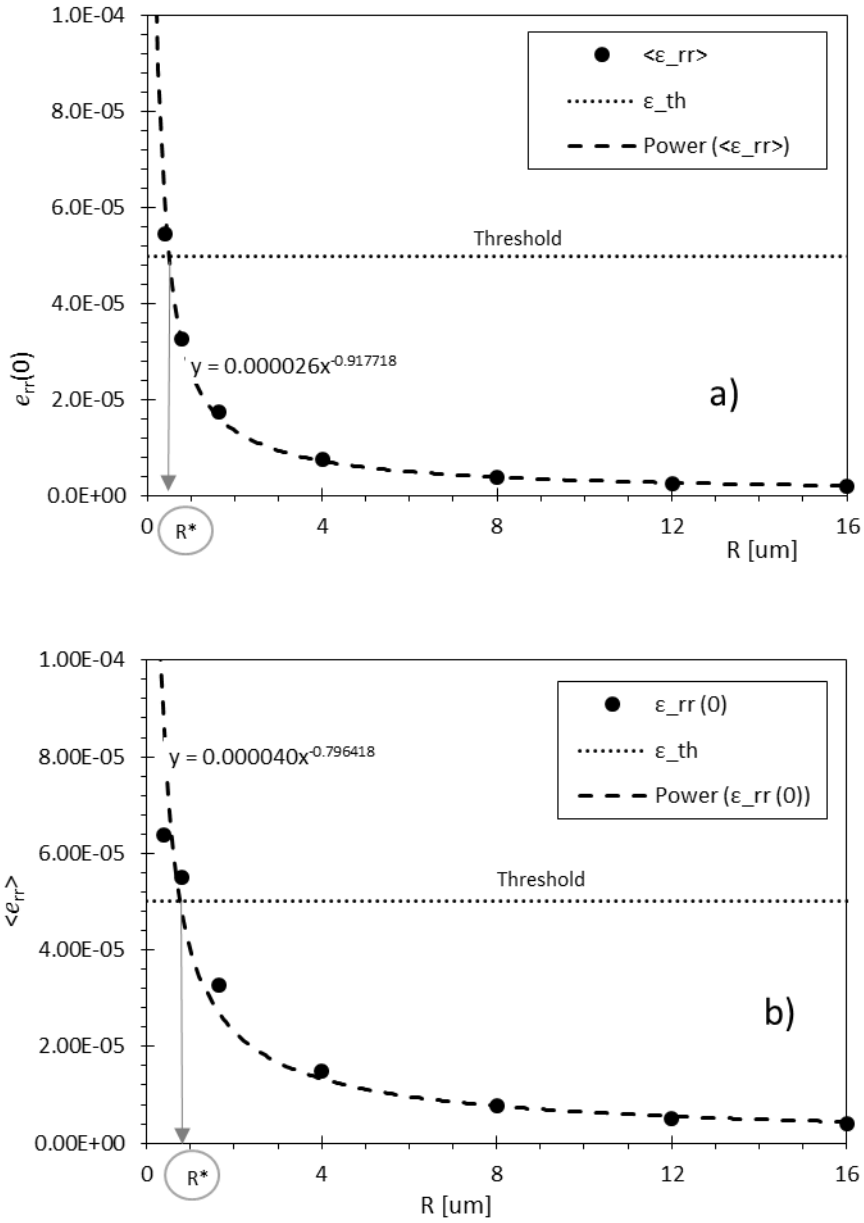

Figure 9. Minimum micro-pillar radius determination. a) Based on the apparent strain at the centre. b) Based on the average strain within the area of 90% radial extension upon at the micro-pillar top surface.

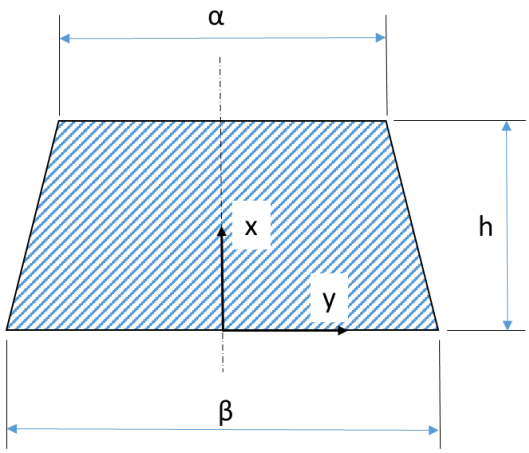

Figure 10. Cantilever cross-section representation